

# Strain Localization Criteria for Viscoplastic Geomaterials

Dawei Xue<sup>1,2</sup>, Ghassan Shahin<sup>2,3</sup>, Xilin Lü<sup>1</sup>, and Giuseppe Buscarnera <sup>\*2</sup>

<sup>1</sup>Key Laboratory of Geotechnical and Underground Engineering of Ministry of Education, Department of Geotechnical Engineering, Tongji University, Shanghai, China

<sup>2</sup>McCormick School of Engineering, Northwestern University, Evanston, IL, USA

<sup>3</sup>Hopkins Extreme Materials Institute, Johns Hopkins University, Baltimore, MD, USA

December 20, 2021

## Abstract

This work presents a viscoplastic localization criterion to detect quasi-instantaneous (i.e., load-induced) and delayed (creep-induced) strain localization in rate-dependent solids. The study is based on the theory of controllability and a viscoplastic description of the mechanical response. Analytical precursors of unstable states are defined through systems of ordinary differential equations (ODEs). The use of the proposed criteria is illustrated at the material point level through a set of strain localization analyses simulating active strain localization of a porous rock. In addition, full-field finite element simulations of compression tests conducted under various pressures are reported to demonstrate the role of local unstable viscoplasticity in the spontaneous propagation of deformation bands under stationary boundary conditions. The study shows that the viscoplastic localization criterion maintains a negative sign as long as the behavior is unstable, i.e., the rate of deformation is accelerating. The sign switch coincides with the transition to decelerating deformation. The analyses revealed that pulses of overstress always emerge in correspondence with the growth of unstable behavior, and the peak matches the transition to stable behavior. The local responses recovered from full-field analyses were consistent with those observed in analyses at material point level and the predictions of the presented theory.

Key Words: Strain Localization, Material Stability, Elasto-viscoplasticity, Unstable Creep

## 1 Introduction

The concentration of permanent strain in relatively narrow bands (i.e, strain localization) is commonly observed both in natural and man-made structures at the verge of failure [1, 2]. In the domain of mechanics, strain localization has been extensively studied both

---

\*g-buscarnera@northwestern.edu

from an experimental [3–6] and a numerical standpoint [7–11]. From a mathematical standpoint, strain localization is typically addressed as a bifurcation problem [12–14], i.e., a condition at which non-homogeneous solutions of the underlying nonlinear field equations become possible without violations of equilibrium or compatibility. At the local material point level, such circumstances typically involve the loss of uniqueness and/or existence of the incremental constitutive response [15]. This type of heterogeneous inelastic deformation can be predicted by the standard strain localization theory [16–22], a framework which has been successfully applied to the analyses of localized failure in geomaterials simulated within the constitutive framework of elastoplasticity [23–27]. In this context, further insight on the mechanisms facilitating strain localization can be gained with the concepts of test controllability [28–31], an approach able to identify impending loss of strength as a function of the static-kinematic conditions prevailing within a deformation band.

The works mentioned above have contributed to the assessment of strain localization in geomaterials. In most cases, however, they are restricted to time- and rate-independent analyses, in which strain localization is caused exclusively by loading processes regardless of the time frame in which they are applied. In contrast with this standard approach, considerable evidence exists time and rate effects may influence the strain localization behavior. This is for instance due to phenomena such as creep, which may degenerate into rapid strain acceleration precurring spontaneous failure [32–36]. Similarly, recent experimental studies have shown that delayed strain localization and accelerating deformations can emerge in ring shear creep tests [37–39]. In the domain of rock mechanics, experiments have shown the accumulation of non-negligible creep under a wide range of confinement conditions, including those conducive of strain localization upon sustained shear. Such effects retain some of the well-known attributes of strain localization in rock, such as pressure-dependence [40–45] and major microstructural alterations [46–50]. In addition, the time-dependence manifesting in the form of creep has been found to lead to the delayed propagation of localized deformation zones [51–55].

Although elastoplasticity is a powerful tool to reproduce the instantaneous inelastic behavior of geomaterials, it cannot capture the above mentioned forms of delayed strain localization emerging both in soils and rocks. By contrast, elasto-viscoplasticity can be used as a powerful tool to model the time-dependent deformation [56–60], thus simulating the delayed growth of deformation bands and the corresponding strain acceleration during creep. In this context, the so-called overstress approach [61] (also referred to as the overstress approach) can be regarded as one of the most widely used frameworks to reproduce the time-dependent response of a wide range of geomaterials [62–66] and regularize ill-posed boundary value problems associated with strain softening [9, 67–69]. Despite these advantages, the analytical identification of delayed localized deformation can be challenging in that the standard strain localization theory and controllability theory are not directly applicable to elasto-viscoplasticity. In this context, recent contributions by Pisanò and Di Prisco [70] provide an alternative methodology to identify strain acceleration in viscoplastic solids subjected to stationary external perturbations. According to this approach, the evolution rate of the response variables is expressed through a system of ordinary differential equations (ODEs). By examining the eigenvalues of the resulting time-varying constitutive operator, transitions from stable to unstable states (and viceversa) can be identified. This methodology can be readily specialized to particular types of geomaterial inelastic deformation issues, as recently shown with reference to the static liquefaction of loose sand [71, 72] and the unstable compaction creep of porous rocks [73, 74].

In this paper, we further expand this line of research by generalizing the approach used

by Shahin et al. [74] for pure compaction bands to any type of shear band kinematics, including those characterized by concurrent shear and volume change. Specifically, we propose a viscoplastic localization criterion to characterize the onset of quasi-instantaneous and delayed strain localization in rate-dependent solids. The proposed criterion is derived for general modes of strain localization, thus encompassing arbitrary inclination of the active band and the consequent deformation kinematics. In analogy with previous studies, such result is obtained by formulating a nonlinear OEDs system to link accelerations of the response variables to their time rate. This strategy enables the derivation of precursors that identify unstable evolution of material response (i.e., accelerating deformation growth) inside the spontaneously propagated strain localized bands under stationary external perturbations. It is shown from strain localization analyses at the material point level and full-field finite element numerical simulations that the presented viscoplastic localization criterion is capable of predicting the onset of different modes of quasi-instantaneous strain localization and identifying the unstable and stable phases of response variables evolution. The paper is structured as follows. Section 2 presents the derivations of the theory in detail. Section 3 describes the constitutive model and model calibration. Section 4 reports on strain localization analyses by constitutive equations at the material point level. Section 5 gives the numerical simulations of a full-field sample. Section 6 outlines the main conclusions of the proposed analyses.

## 2 Theoretical Interpretation of Strain Localization

Material inelasticity in the form of delayed strain localization featured by strain jump, i.e., accelerating strain evolution, can be found under stationary external perturbations [51]. In order to examine such events through the lens of viscoplasticity, it is convenient to refer to the constitutive response inside the localized band. Let us therefore consider the following partition:

$$\begin{Bmatrix} \dot{\sigma}_\alpha \\ \dot{\sigma}_\beta \end{Bmatrix} = \begin{bmatrix} D_{\alpha\alpha}^e & D_{\alpha\beta}^e \\ D_{\beta\alpha}^e & D_{\beta\beta}^e \end{bmatrix} \begin{Bmatrix} \dot{\epsilon}_\alpha - \dot{\epsilon}_\alpha^{vp} \\ \dot{\epsilon}_\beta - \dot{\epsilon}_\beta^{vp} \end{Bmatrix} \quad (1)$$

where,  $\dot{\sigma}_\alpha$  and  $\dot{\epsilon}_\beta$  are the controlled loading variables, while  $\dot{\epsilon}_\alpha$  and  $\dot{\sigma}_\beta$  are the response variables. By considering the deformation kinematics of the strain localized bands, i.e., intense localized shearing inside a thin area, it is reasonable to assume that the deformation kinematic inside the bands can be described as a simple shear mode [31] (Fig. 1). As a result, the control parameters are expressed as  $\{\dot{\sigma}_\alpha \ \dot{\epsilon}_\beta\} = \{\dot{\sigma}_{11} \ \dot{\tau}_{12} \ \dot{\epsilon}_{22} \ \dot{\epsilon}_{33} \ \dot{\gamma}_{23} \ \dot{\gamma}_{13}\}^T$ , while the response variables are expressed as  $\{\dot{\epsilon}_\alpha \ \dot{\sigma}_\beta\} = \{\dot{\epsilon}_{11} \ \dot{\gamma}_{12} \ \dot{\sigma}_{22} \ \dot{\sigma}_{33} \ \dot{\tau}_{23} \ \dot{\tau}_{13}\}^T$  (see Appendix A for details).  $D_{\alpha\alpha}^e$ ,  $D_{\alpha\beta}^e$ ,  $D_{\beta\alpha}^e$ , and  $D_{\beta\beta}^e$  are the partitioned elastic tensors, which can be obtained from the conventional elastic tensor through Appendix B.  $\dot{\epsilon}_\alpha^{vp}$  and  $\dot{\epsilon}_\beta^{vp}$  are the partitioned viscoplastic strain rate components.

In this paper, the viscoplastic behavior is modeled using the overstress approach proposed by Perzyna [61]. This approach used a viscous nucleus function,  $\Phi$ , that depends on the distance between the stress state exceeding the elastic domain (the so-called overstress) and the yield surface. As a result, the viscoplastic strain rate can be expressed as:

$$\begin{Bmatrix} \dot{\epsilon}_\alpha^{vp} \\ \dot{\epsilon}_\beta^{vp} \end{Bmatrix} = \Phi(f) \begin{Bmatrix} \frac{\partial g}{\partial \sigma_\alpha} \\ \frac{\partial g}{\partial \sigma_\beta} \end{Bmatrix} \quad (2)$$

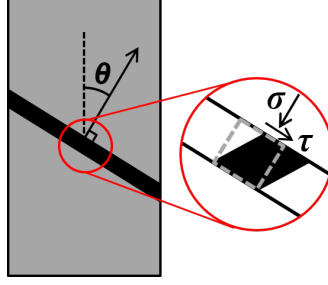


Figure 1: Schematic diagram of strain localization, inside which the simple shear kinematics is shown. Rotation is applied by  $\theta$ , the angle between normal direction of the localized band and the direction of the maximum compressive stress.

where, the function  $g(\boldsymbol{\sigma})$  is the plastic potential. This formulation allows for the incorporation of time effects associated with a number of unspecified microscopic processes, which may include microscopic inertia, wave propagation, and stress-controlled reaction kinetics at crack surfaces [75]. In order to conduct strain localization analyses, the inclination of the localized band should be considered (Fig. 1). To this end, a rotated reference system needs to be further taken into account. The rotation is applied by an angle  $\theta$ , i.e, the angle between normal direction of the localized band and the direction of the maximum compressive stress, and can be imposed using a directional cosine matrix,  $\mathbf{T}$  (Appendix A). Correspondingly, the rotated stress rate vector, strain rate vector and elastic constitutive tensor can be expressed as:

$$\dot{\boldsymbol{\sigma}}^R = \mathbf{T} \cdot \dot{\boldsymbol{\sigma}} \quad (3a)$$

$$\dot{\boldsymbol{\epsilon}}^R = \{\mathbf{T}^T\}^{-1} \cdot \dot{\boldsymbol{\epsilon}} \quad (3b)$$

$$\mathbf{D}^{e,R} = \mathbf{T} \mathbf{D}^e \mathbf{T}^T \quad (3c)$$

It is readily apparent that Eqs. 1 through 3 describe the simple shear constitutive response in the rotated reference system. Using these equations, the rate-dependent response variables  $\dot{\boldsymbol{\epsilon}}_{\alpha}^R$  and  $\dot{\boldsymbol{\sigma}}_{\beta}^R$  can be derived as follows:

$$\dot{\boldsymbol{\epsilon}}_{\alpha}^R = \Phi \frac{\partial g}{\partial \boldsymbol{\sigma}_{\alpha}^R} + (\mathbf{D}_{\alpha\alpha}^{e,R})^{-1} \dot{\boldsymbol{\sigma}}_{\alpha}^R - (\mathbf{D}_{\alpha\alpha}^{e,R})^{-1} \mathbf{D}_{\alpha\beta}^{e,R} \left( \dot{\boldsymbol{\epsilon}}_{\beta}^R - \Phi \frac{\partial g}{\partial \boldsymbol{\sigma}_{\beta}^R} \right) \quad (4)$$

$$\dot{\boldsymbol{\sigma}}_{\beta}^R = \mathbf{D}_{\beta\alpha}^{e,R} (\mathbf{D}_{\alpha\alpha}^{e,R})^{-1} \dot{\boldsymbol{\sigma}}_{\alpha}^R + \left( \mathbf{D}_{\beta\beta}^{e,R} + \mathbf{D}_{\beta\alpha}^{e,R} (\mathbf{D}_{\alpha\alpha}^{e,R})^{-1} \mathbf{D}_{\alpha\beta}^{e,R} \right) \left( \dot{\boldsymbol{\epsilon}}_{\beta}^R - \Phi \frac{\partial g}{\partial \boldsymbol{\sigma}_{\beta}^R} \right) \quad (5)$$

which can be expressed in the following matrix form:

$$\begin{Bmatrix} \dot{\boldsymbol{\epsilon}}_{\alpha}^R \\ \dot{\boldsymbol{\sigma}}_{\beta}^R \end{Bmatrix} = \mathbf{A} \begin{Bmatrix} \dot{\boldsymbol{\sigma}}_{\alpha}^R \\ \dot{\boldsymbol{\epsilon}}_{\beta}^R \end{Bmatrix} + \Phi \mathbf{B} \begin{Bmatrix} \frac{\partial g}{\partial \boldsymbol{\sigma}_{\alpha}^R} \\ \frac{\partial g}{\partial \boldsymbol{\sigma}_{\beta}^R} \end{Bmatrix} \quad (6)$$

where,

$$\mathbf{A} = \begin{bmatrix} \mathbf{A}_{\alpha\alpha} & \mathbf{A}_{\alpha\beta} \\ \mathbf{A}_{\beta\alpha} & \mathbf{A}_{\beta\beta} \end{bmatrix} = \begin{bmatrix} (\mathbf{D}_{\alpha\alpha}^{e,R})^{-1} & -(\mathbf{D}_{\alpha\alpha}^{e,R})^{-1} \mathbf{D}_{\alpha\beta}^{e,R} \\ \mathbf{D}_{\beta\alpha}^{e,R} (\mathbf{D}_{\alpha\alpha}^{e,R})^{-1} & \mathbf{D}_{\beta\beta}^{e,R} + \mathbf{D}_{\beta\alpha}^{e,R} (\mathbf{D}_{\alpha\alpha}^{e,R})^{-1} \mathbf{D}_{\alpha\beta}^{e,R} \end{bmatrix} \quad (7a)$$

$$B = \begin{bmatrix} B_{\alpha\alpha} & B_{\alpha\beta} \\ B_{\beta\alpha} & B_{\beta\beta} \end{bmatrix} = \begin{bmatrix} I_{\alpha\alpha} & -A_{\beta\alpha} \\ O_{\beta\alpha} & -A_{\beta\beta} \end{bmatrix} \quad (7b)$$

In the above expressions,  $I_{\alpha\alpha}$  is the identity matrix, and  $O_{\beta\alpha}$  is a null matrix.

By formulating the acceleration of the response variables, i.e.,  $\ddot{\epsilon}_{\alpha}^R$  and  $\ddot{\sigma}_{\beta}^R$ , the following set of equations can be obtained:

$$\ddot{\epsilon}_{\alpha}^R = F_{\epsilon}^a + \frac{d\Phi}{dt} \left( \frac{\partial g}{\partial \sigma_{\alpha}^R} + B_{\alpha\beta} \frac{\partial g}{\partial \sigma_{\beta}^R} \right) + \Phi \left( \frac{d}{dt} \frac{\partial g}{\partial \sigma_{\alpha}^R} + \frac{d}{dt} B_{\alpha\beta} \frac{\partial g}{\partial \sigma_{\beta}^R} \right) \quad (8)$$

$$\ddot{\sigma}_{\beta}^R = F_{\sigma}^a + \frac{d\Phi}{dt} B_{\beta\beta} \frac{\partial g}{\partial \sigma_{\beta}^R} + \Phi \frac{d}{dt} B_{\beta\beta} \frac{\partial g}{\partial \sigma_{\beta}^R} \quad (9)$$

where,  $F_{\epsilon}^a = A_{\alpha\alpha} \ddot{\sigma}_{\alpha}^R + A_{\alpha\beta} \ddot{\epsilon}_{\beta}^R$ , and  $F_{\sigma}^a = A_{\beta\alpha} \ddot{\sigma}_{\alpha}^R + A_{\beta\beta} \ddot{\epsilon}_{\beta}^R$ .

In Eqs. 8 and 9, the time derivatives of the viscous nucleus is derived as:

$$\frac{d\Phi}{dt} = -\frac{\partial \Phi}{\partial f} \underbrace{\left( H\Phi - H_{\chi}\Phi - \underbrace{\left( \frac{\partial f}{\partial \sigma_{\alpha}^R} + \frac{\partial f}{\partial \sigma_{\beta}^R} A_{\beta\alpha} \right) \dot{\sigma}_{\alpha}^R + \frac{\partial f}{\partial \sigma_{\beta}^R} A_{\beta\beta} \dot{\epsilon}_{\beta}^R}_{H_{\sigma\epsilon}} \right)}_{H_{IN}\Phi} \quad (10)$$

where,  $H = -\frac{\partial f}{\partial \epsilon^p} \frac{\partial g}{\partial \sigma}$  is the hardening modulus that can be computed according to a specific constitutive behavior, and  $H_{\chi}$  is expressed as follows:

$$H_{\chi} = -\frac{\partial f}{\partial \sigma_{\beta}^R} A_{\beta\beta} \frac{\partial g}{\partial \sigma_{\beta}^R} \quad (11)$$

In the above equation,  $H_{\chi}$  represents a term that reflects the imposed control conditions (i.e., the combination of imposed stress and strain increments). For these reasons, this term is referred to as modulus of controllability [30]. For the analyses conducted in this work,  $H_{\chi}$  has been specialized to simple shear control conditions.

In Eqs. 8 and 9, the time derivative of the plastic potential can be developed as follows:

$$\frac{d}{dt} \frac{\partial g}{\partial \sigma_{\alpha}^R} + \frac{d}{dt} B_{\alpha\beta} \frac{\partial g}{\partial \sigma_{\beta}^R} = F_{\epsilon}^b + \left( \frac{\partial^2 g}{\partial \sigma_{\alpha}^R \partial \sigma_{\beta}^R} + B_{\alpha\beta} \frac{\partial^2 g}{\partial \sigma_{\beta}^R \partial \sigma_{\beta}^R} \right) \dot{\sigma}_{\beta}^R \quad (12)$$

$$\frac{d}{dt} B_{\beta\beta} \frac{\partial g}{\partial \sigma_{\beta}^R} = F_{\sigma}^b + B_{\beta\beta} \frac{\partial^2 g}{\partial \sigma_{\beta}^R \partial \sigma_{\beta}^R} \dot{\sigma}_{\beta}^R \quad (13)$$

where,  $F_{\epsilon}^b = \left( \frac{\partial^2 g}{\partial \sigma_{\alpha}^R \partial \sigma_{\alpha}^R} + B_{\alpha\beta} \frac{\partial^2 g}{\partial \sigma_{\beta}^R \partial \sigma_{\alpha}^R} \right) \dot{\sigma}_{\alpha}^R$ , and  $F_{\sigma}^b = B_{\beta\beta} \frac{\partial^2 g}{\partial \sigma_{\beta}^R \partial \sigma_{\alpha}^R} \dot{\sigma}_{\alpha}^R$

Using Eqs. 6 through 13, the acceleration of the response variables can be rewritten as:

$$\begin{Bmatrix} \ddot{\epsilon}_{\alpha}^R \\ \ddot{\sigma}_{\beta}^R \end{Bmatrix} = F + \left( -\frac{\partial \Phi}{\partial f} H_{IN} \right) \begin{bmatrix} B_{\alpha\alpha} & B_{\alpha\beta} \\ B_{\beta\alpha} & B_{\beta\beta} \end{bmatrix} \begin{Bmatrix} \Phi \frac{\partial g}{\partial \sigma_{\alpha}^R} \\ \Phi \frac{\partial g}{\partial \sigma_{\beta}^R} \end{Bmatrix} + \Phi \begin{bmatrix} \frac{\partial^2 g}{\partial \sigma_{\alpha}^R \partial \sigma_{\beta}^R} + B_{\alpha\beta} \frac{\partial^2 g}{\partial \sigma_{\beta}^R \partial \sigma_{\beta}^R} \\ B_{\beta\beta} \frac{\partial^2 g}{\partial \sigma_{\beta}^R \partial \sigma_{\beta}^R} \end{bmatrix} \dot{\sigma}_{\beta}^R \quad (14)$$

where,  $\mathbf{F} = \begin{Bmatrix} \mathbf{F}_\varepsilon^a + \Phi \mathbf{F}_\varepsilon^b \\ \mathbf{F}_\sigma^a + \Phi \mathbf{F}_\sigma^b \end{Bmatrix}$  is a vector of forcing terms.

Considering the constraints of simple shear deformation, i.e.,  $\dot{\varepsilon}_\beta^R = \mathbf{0}$  (Appendix A), and the creep condition, i.e.,  $\dot{\sigma}_\alpha^R = \mathbf{0}$  (also referred to as stationary external perturbations), the underlying ODEs system governing the inclined simple shear deformation process can be finally obtained as:

$$\begin{Bmatrix} \ddot{\varepsilon}_\alpha^R \\ \ddot{\sigma}_\beta^R \end{Bmatrix} = \mathbf{Z} \begin{Bmatrix} \dot{\varepsilon}_\alpha^R \\ \dot{\sigma}_\beta^R \end{Bmatrix} + \mathbf{F} \quad (15)$$

where,

$$\mathbf{Z} = \begin{bmatrix} \mathbf{Z}_{\alpha\alpha} & \mathbf{Z}_{\alpha\beta} \\ \mathbf{Z}_{\beta\alpha} & \mathbf{Z}_{\beta\beta} \end{bmatrix} = \begin{bmatrix} -\frac{\partial \Phi}{\partial f} H_{IN} \mathbf{I}_{\alpha\alpha} & \Phi \left( \frac{\partial^2 g}{\partial \sigma_\alpha^R \partial \sigma_\beta^R} + \mathbf{B}_{\alpha\beta} \frac{\partial^2 g}{\partial \sigma_\beta^R} \right) \\ \mathbf{O}_{\beta\alpha} & -\frac{\partial \Phi}{\partial f} H_{IN} \mathbf{I}_{\beta\beta} - \Phi \mathbf{A}_{\beta\beta} \frac{\partial^2 g}{\partial \sigma_\beta^R} \end{bmatrix} \quad (16)$$

In the above expression,  $\mathbf{I}_{\beta\beta}$  is the identity matrix.

In Eq. 15,  $\mathbf{F}$  and  $H_{\sigma\varepsilon}$  vanish for creep loading conditions [70]. It is apparent that the ODEs system summarized in Eq. 14 governs the acceleration of response variables through the time-varying matrix  $\mathbf{Z}$ . As a result, the acceleration of response variables under constant stress state (i.e., creep loading condition) is controlled by the eigenvalues of  $\mathbf{Z}$ . By inspecting Eq. 15, it can be noticed that negative eigenvalues cause a decelerating evolution of the response variables rate, which is seen as a stable response, while positive eigenvalues bring about an accelerating evolution of the response variables rate, which is seen as an unstable response. Therefore, in order to evaluate the stability of the ODEs system, the sign of the eigenvalues of  $\mathbf{Z}$  needs to be tracked. Obviously, the eigenvalues of  $\mathbf{Z}$  consist of the eigenvalues of  $\mathbf{Z}_{\alpha\alpha}$  and  $\mathbf{Z}_{\beta\beta}$ , the former is a diagonal matrix and the latter is the sum of a diagonal matrix and a full matrix. Each  $i^{th}$  eigenvalue  $\lambda_{\alpha\alpha}^i$  of  $\mathbf{Z}_{\alpha\alpha}$  can be expressed as:

$$\lambda_{\alpha\alpha}^i = -\frac{\partial \Phi}{\partial f} (H - H_\chi) \in \Lambda(\mathbf{Z}_{\alpha\alpha}) \quad (17)$$

and each  $i^{th}$  eigenvalue  $\lambda_{\beta\beta}^i$  of matrix  $\mathbf{Z}_{\beta\beta}$  can be expressed as:

$$\lambda_{\beta\beta}^i = -\frac{\partial \Phi}{\partial f} (H - H_\chi) - M^i \in \Lambda(\mathbf{Z}_{\beta\beta}) \quad (18)$$

where,  $M^i$  are eigenvalues of matrix  $\Phi \mathbf{A}_{\beta\beta} \frac{\partial^2 g}{\partial \sigma_\beta^R}$ , e.g.,

$$M^i \in \Lambda(\mathbf{C}) \quad \mathbf{C} = \Phi \mathbf{A}_{\beta\beta} \frac{\partial^2 g}{\partial \sigma_\beta^R} \quad (19)$$

$M^i$  are all positive because  $\mathbf{C}$  is positive definite under the condition that the plastic potential  $g$  is convex [70], indicating that  $\lambda_{\alpha\alpha}^i > \lambda_{\beta\beta}^i$  is always fulfilled during creep. This means that the response variables evolve stably, i.e., show a decaying evolution, under the condition that  $H_{IN} = H - H_\chi > 0$  (since all eigenvalues of  $\mathbf{Z}$  are negative). By contrast, when  $H_{IN} = H - H_\chi < 0$ , an accelerating evolution of the corresponding response variable rate could happen (since some of the eigenvalues become positive), which indicates

an unstable response. As a result,  $H_{IN} = H - H_\chi > 0$  acts as a sufficient condition for viscoplastic stability.

It should be noted here that the viscoplastic localization criterion  $H_{IN}$  summarized in this section can also be derived from the controllability theory under the elastoplastic framework (see [30]). This criterion is equivalent to the standard theory [16, 76] for identification of quasi-instantaneous (i.e., load-induced) strain localization in rate-independent materials, in that both predict the inception of localized deformation by capturing the conditions fulfilled by the material at the point in which the acoustic tensor exhibits singularity (see [31]). However, standard strain localization theory is not applicable to the detection of delayed (creep-induced) strain localization in rate-dependent solids, while through the mathematical method in this section, the criterion described in this paper can be extended to detect the creep-induced acceleration of the response variables inside deformation bands.

In the following, the applicability of the theory on interpreting of quasi-instantaneous and delayed strain localization will be verified using analyses at the material point level and full-field numerical simulations of a full-field sample. For this purpose, the theory will be linked to a specific elasto-viscoplastic constitutive model.

### 3 Constitutive Modeling

#### 3.1 Mathematical Formalism

The analytical framework discussed above is here combined with a specific strain-hardening viscoplastic constitutive model. The elastoplastic version of this model was proposed by Nova and co-workers [77, 78]. The model incorporates hardening and softening mechanisms to replicate the active processes in soft rocks/hard soils. Extensive work has illustrated its ability to capture the mechanical response of sands [31] and porous rocks [9, 25]. Recent work has also shown its ability to capture the time-dependent behavior of sandstones [74]. Both the yield function and plastic potential are described by the expression proposed by Lagioia et al. [79], given by:

$$\left. \begin{matrix} f \\ g \end{matrix} \right\} = \left( A_h^{K_{1h}/C_h} \cdot B_h^{-K_{2h}/C_h} \right) P - P_c^* \quad (20a)$$

$$A_h = 1 + \frac{\eta^*}{K_{1h}M_h} \quad (20b)$$

$$B_h = 1 + \frac{\eta^*}{K_{2h}M_h} \quad (20c)$$

$$C_h = (1 - \mu_h)(K_{1h} - K_{2h}) \quad (20d)$$

where, the function  $K_{1h,2h}$  is defined as:

$$K_{1h,2h} = \frac{\mu_h(1 - \alpha_h)}{2(1 - \mu_h)} \left( 1 \pm \sqrt{1 - \frac{4\alpha_h(1 - \mu_h)}{\mu_h(1 - \alpha_h)^2}} \right) \quad (21)$$

where,  $p = \sigma_{kk}/3$  is the mean stress (positive in pressure),  $q = \sqrt{3/2s_{ij}s_{ij}}$  is the equivalent shear stress,  $s_{ij} = \sigma_{ij} - p\delta_{ij}$  is the deviatoric stress, and  $\eta^* = q/(p + P_t)$  is modified stress ratio. The variable  $P_c$  is the hydrostatic yield stress and is formulated by combing the

hardening variables  $P_s$  and  $P_m$ , i.e.,  $P_c^* = P_s + P_m + P_t$ , where  $P_t = \kappa P_m$  is the tensile stress.  $P_s$  and  $P_m$  reflect the contributions of the skeleton packing and intergranular cementation. The shape of the two surfaces in Eqs. 20 and 21 is controlled by the parameters,  $M_h$ ,  $\mu_h$ , and  $\alpha_h$ , for which the subscript  $h$  makes reference to either the yield surface ( $h \Rightarrow f$ , e.g.,  $M_f$ ,  $\mu_f$ , and  $\alpha_f$ ) or the plastic potential ( $h \Rightarrow g$ , e.g.,  $M_g$ ,  $\mu_g$ , and  $\alpha_g$ ). These parameters can be used in a versatile manner to replicate different shapes of the elastic domain and non-associative plastic flow, and can be readily calibrated based on the experimental data. The hardening rules of this model can be expressed as:

$$\dot{P}_s = \frac{P_s}{B_p} \dot{\varepsilon}_v^p \quad (22)$$

$$\dot{P}_m = -\rho_m P_m (|\dot{\varepsilon}_v^p| + \xi_m \dot{\varepsilon}_s^p) \quad (23)$$

where,  $B_p$ ,  $\rho_m$ , and  $\xi_m$  are material parameters. In the above expressions,  $P_s$  plays the role of the preconsolidation pressure, similar to the hardening law used in Cam-clay models [80]. By using the hypothesis of material isotropy, the evolution of  $P_s$  is associated with the volumetric plastic strain rate, which reflects hardening mechanisms reflecting irreversible porosity changes. Such formulation of  $P_s$  has been successfully applied to capture hardening behavior in both saturated and unsaturated soils [31, 81]. By contrast,  $P_m$  introduces softening mechanisms due to volumetric and deviatoric plastic strain. As proposed by Nova [78], the variable  $P_m$  accounts for the strain-softening mechanisms provided by interparticle bonding degradation and has been successfully used to reproduce inelastic behavior in cemented granular materials [9]. The interplay between the hardening variables leads to a contraction or expansion of the yield surface, which affects the localization processes and post-localization deformation. This constitutive law can be used in its original rate-independent form, according to which the plastic strains are obtained through a standard consistency condition, as follows:

$$\dot{\varepsilon}_{ij}^p = \Lambda \frac{\partial g}{\partial \sigma_{ij}} \quad (24)$$

where,  $\Lambda$  is a non-negative plastic multiplier. A Rate-dependent mechanical response can be obtained by converting the model into a viscoplastic form. For this purpose, the plastic flow rule in Eq. 24 can be modified by replacing the plastic multiplier  $\Lambda$  with an overstress function  $\Phi(f)$ , as follows:

$$\dot{\varepsilon}_{ij}^{vp} = \Phi(f) \frac{\partial g}{\partial \sigma_{ij}} = \frac{1}{\omega} \left[ \frac{\langle f \rangle}{P_{c0}} \right] \frac{\partial g}{\partial \sigma_{ij}} \quad (25)$$

where,  $P_{c0}$  is the initial hydrostatic yielding stress, the symbol  $\langle \bullet \rangle$  indicates the Macaulay brackets, and  $\omega$  is the viscosity factor. The constitutive equations are completed by a linear elastic relation for the reversible part of the strain increments, as follows:

$$\dot{\sigma}_{ij} = D_{ijkl}^e \varepsilon_{kl}^e \quad (26)$$

$$D_{ijkl}^e = \left( K - \frac{2}{3}G \right) \delta_{ij} \delta_{kl} + G (\delta_{ik} \delta_{jl} + \delta_{il} \delta_{jk}) \quad (27)$$

where,  $K$  and  $G$  are bulk modulus and shear modulus, respectively.

### 3.2 Model Calibration

Based on the standard strain localization theory [16], Marinelli and Buscarnera [25] proposed a calibration procedure for the selected constitutive model. In their work, the model was calibrated with reference to numerous sandstones. Here, the model calibration for Berea sandstone (Table 1) is used to evaluate the applicability of the viscoplastic localization criterion since this material exhibits different modes of compaction strain localization in a wide range of confinements, as show in the experimental studies reported by Baud et al. [42, 43]. It should be noted that, although the theory presented in this paper can encompass strain localization processes characterized by either compaction or dilation within the active localization zone, here only the case of compactive shear bands has been considered, thus benefiting from previous calibration efforts specific for high porosity rocks (e.g., [25, 74]).

Table 1: List of the constitutive model parameters for Berea sandstone calibrated by Marinelli and Buscarnera [25].

Symbol	Definition of the parameters	Berea
$K$ [Mpa] (Eq. 27)	Bulk modulus	9550
$G$ [Mpa] (Eq. 27)	Shear modulus	7000
$\mu_f$ (Eq. 21)	Shape parameter of yield surface	1.3
$\alpha_f$ (Eq. 21)	Shape parameter of yield surface	0.2
$M_f$ (Eq. 21)	Shape parameter of yield surface	1.02
$\kappa$	Expansion of yield surface in the tensile stress domain	0.025
$\mu_g$ (Eq. 21)	Shape parameter of plastic potential	2
$\alpha_g$ (Eq. 21)	Shape parameter of plastic potential	0.2
$M_g$ (Eq. 21)	Shape parameter of plastic potential	1.88
$P_{s0}$ [Mpa]	Size of the initial elastic domain for cohesionless medium	80
$P_{m0}$ [Mpa]	Expansion in size of the elastic domain for cemented media	295
$B_p$ (Eq. 22)	Isotropic plastic compressibility	0.03
$\rho_m$ (Eq. 23)	Parameter governing volumetric destructuration	3.7
$\xi_m$ (Eq. 23)	Parameter governing deviatoric destructuration	0.5
$\omega$ [s] (Eq. 25)	Viscosity factor	100

Through the standard strain localization theory [16], it is possible to identify conditions susceptible “strain localization”. Within the elastoplastic framework, the localization criterion can be expressed as follows:

$$A(\theta) = \det \left[ n_j(\theta) D_{ijkl}^{ep} n_l(\theta) \right] < 0 \quad (28)$$

where,  $\theta$  is the inclination of the strain localized bands, i.e., the angle between the unit vector,  $n_j$ , normal direction of the compaction bands and the direction of the maximum compressive stress (Fig. 1),  $D_{ijkl}^{ep}$  is the elastoplastic constitutive tensor. Vanishing or negative values of  $A(\theta)$ , i.e.,  $A(\theta) \leq 0$ , can be used to detect localized deformation modes at different band inclinations  $\theta$ . The most likely band inclination  $\theta_{min}$  can be assessed according to the minimum of the function  $A(\theta)$ , i.e.,  $A(\theta_{min}) = \min(A)$ . Fig. 2a shows the calibrated “localization domains” on yield surface. The thick green, blue, and red lines represent the formation of shear bands ( $A(\theta_{min}) < 0 < A(\theta = 0)$ ), shear-enhanced compaction bands ( $A(\theta_{min}) < A(\theta = 0) < 0$ ), and pure compaction bands ( $A(\theta_{min}) = A(\theta = 0) < 0$ ), respectively. The predicted mechanical response of triaxial compression

tests is shown in Fig. 2b. The comparison between experimental data and model simulations matched satisfactorily.

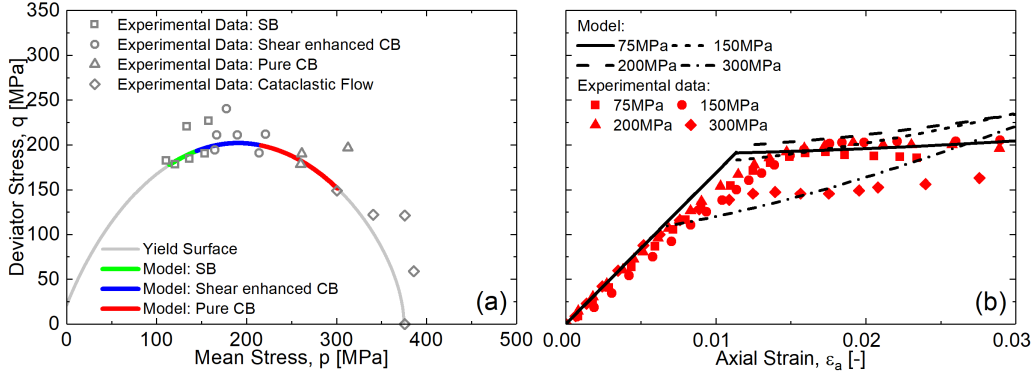


Figure 2: Comparison between experimental data and model simulations for Berea sandstone: (a) Yield surface and strain localization domains and (b) Mechanical response of triaxial compression tests. SB indicates shear bands, and CB indicates compaction bands

## 4 Identification of Strain Localization at the Constitutive Level

This section discusses analyses of strain localization at the material point level with the goal to illustrate the use of the proposed controllability criteria. The simulations consist of two stages: (1) a loading stage bringing the stress state in the proximity of the initial yield surface and (2) a creep stage simulating strain evolution over time. For the first stage, plane strain constraints are selected. In order to restrict the pre-creep stress conditions to a compression regime (i.e., Lode angle =  $30^\circ$ ), horizontal displacements in the plane are constrained. As for the creep stage, when the stress state reaches the initial yield surface, the viscoplastic localization criterion for a range of possible inclinations may vanish or turn negative (i.e.,  $H_{IN}(\theta) \leq 0$ ) and a new control condition is then imposed to conduct a creep simulation. This new control condition implies simple shear conditions active within a deformation band with inclination  $\theta_{min}$ . Such angle corresponds to the minimum value of  $H_{IN}(\theta)$ , and hence with the deformation band that is most likely to be triggered upon incremental loading. It should be noted that the use of the term “creep” in the context of strain localization analyses focuses on the possibility of developing deformation components compatible with the kinematics of the band (i.e., normal and/or tangential to the plane of the considered band) once their corresponding stress components are kept constant. To ease the practical use of  $H_{IN}(\theta)$  for readers, technical details for computing the modulus of controllability  $H_\chi$  is shown in Appendix. B

To study the material response resulting from different initial conditions, four stress paths starting from different confining pressures (i.e., P1 ( $P_0 = 10MPa$ ), P2 ( $P_0 = 40MPa$ ), P3 ( $P_0 = 140MPa$ ), and P4 ( $P_0 = 250MPa$ )) are selected to bring the stress state in the proximity of the initial yield surface, thus intersecting the regions of unstable shear bands, shear-enhanced compaction bands, and pure compaction bands, and finally the region outside the domains of strain localization (Fig. 3). The points of intersection

are numbered from I through IV, respectively. In addition to stress paths inside the elastic domain, Fig. 3 also shows the stress paths during creep stage and the corresponding expansions of the yield surface. P1, P2, and P3 show very clear expansions of yield surface featured by a similar relative movement between the yield surface and the stress state, which in agreement to standard viscoplastic formulation is allowed to lay outside the elastic domain (i.e., non-zero overstress). Specifically, the growth of the stress state is initially faster due to the initial value of overstress, eventually moving at a slower pace because of the expansion of the yield surface. P4, however, only shows slight expansion of the yield surface because of the limited values of overstress at that state, as well as of a predicted stress path quasi-tangential to the local yield surface (i.e., stress path proximal to neutral loading). Fig. 4 shows the viscoplastic localization criterion calculated for planes with inclination from  $-90^\circ$  through  $+90^\circ$  for points I through IV. The predicted modes of strain localization based on the presented viscoplastic localization criterion match with those predicted based on the standard strain localization theory. Specifically, both theories indicate possibilities of shear banding with  $\pm 30^\circ$  inclination at point I, shear enhanced compaction banding with  $\pm 21^\circ$  at II, and pure compaction banding at III (see Figs. 4a through 4c). By contrast, point IV is outside the localization domain, and the viscoplastic localization criterion shows positive values for all inclinations, which suggests that strain localization does not tend to happen (Fig. 4d). It is readily apparent that the results presented in Fig. 4 indicate that the proposed criterion can satisfactorily detect and interpret quasi-instantaneous strain localization.

The evolution of creep axial strain is presented in Fig. 5a, which is plotted versus the normalized time  $T/T_c$ , i.e., the ratio between the current time  $T$  and total creep time  $T_c$ . P1, P2, and P3 show an initially accelerating evolution of creep axial strain rate followed by a decelerating evolution of creep axial strain rate, and finally, the creep strain rates of all three paths tend to be zero. The creep strain rate of P4, however, always exhibits decaying trend, and finally stabilize to zero. The corresponding histories of deviatoric stress for P1, P2, P3, and P4 show similar trends to the evolution of creep strain (Fig. 5b). P1, P2, and P3 show a rapidly growing phase followed by a decaying phase which finally moves towards stable conditions. The former corresponds to the accelerating evolution of the creep axial strain rate, while the latter corresponds to the decelerating evolution of the creep axial strain rate. The evolution trend of deviatoric stress for P4 also shows the same decaying mode of the creep strain evolution. As mentioned in the previous paragraph, P1, P2, and P3 show a mismatch of the evolution rate of stress state and yield surface. This mismatch is featured by the relative movement between the stress state and the yield surface and, in fact, it determines whether the strain rate accelerates or decelerates. As a result, the viscous nucleus,  $\Phi$ , measuring the relative movement between the stress state and yield surface can be used to identify the strain accelerating and decelerating phases. Fig. 5c shows the evolution of the viscous nucleus (i.e., a function closely dependent on the overstress) for all stress paths. The increasing of overstress corresponds to the strain accelerating phase, see P1, P2, and P3, while the decreasing of overstress indicates the strain decelerating phase, see P1, P2, P3, and P4. For P1, P2, and P3, the peak of overstress histories coincides with the transition point of strain accelerating and decelerating phase, as marked by red solid square, circle, and triangle, respectively. The overstress history of P4 keeps decreasing through out the creep stage, which is in agreement with the decaying strain rate. It is therefore readily apparent that the viscoplastic localization criterion proposed in this paper is efficient in interpreting the dynamics of both stable and unstable creep in geomaterials susceptible to strain localization. As shown in Fig. 5d, the viscoplastic localization criterion,

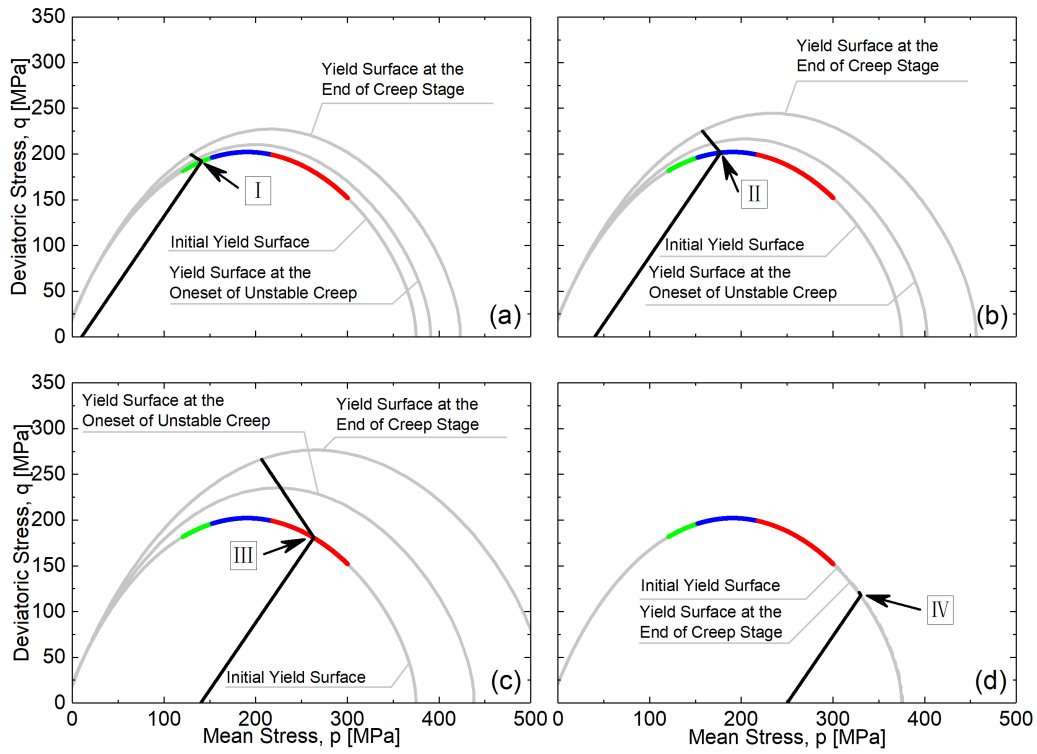


Figure 3: Stress paths of strain localization analyses by constitutive equations: (a) Stress path P1 ( $P_0 = 10\text{MPa}$ ) intersects the yield surface at Point I inside the shear localization domain (i.e., green region), (b) Stress path P2 ( $P_0 = 40\text{MPa}$ ) intersects the yield surface at Point II inside the shear-enhanced strain localization domain (i.e., blue region), (c) Stress path P3 ( $P_0 = 140\text{MPa}$ ) intersects the yield surface at Point III inside the pure strain localization domain (i.e., red region), and (d) Stress path P4 ( $P_0 = 250\text{MPa}$ ) intersects the yield surface at Point IV outside the localization domain.

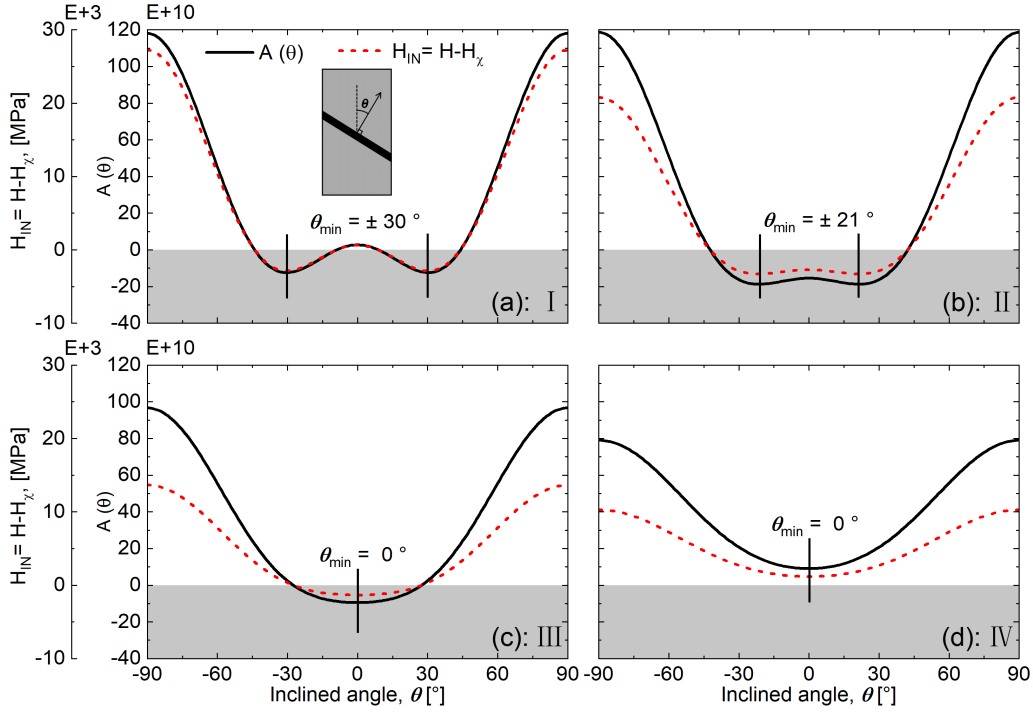


Figure 4: Comparison between the standard strain localization theory and the presented viscoplastic localization criterion: (a) Point I, (b) Point II, (c) Point III, and (d) Point IV

$H_{IN}$ , of P1, P2, and P3 is initially negative, indicating positive eigenvalues of the matrix  $\mathbf{Z}$  in Eq. 15. This result underpins a tendency to strain acceleration (i.e, unstable creep). As creep continues, however,  $H_{IN}$  experienced a change in sign (from negative to positive), corresponding to which is the strain deceleration in conjunction with a decaying evolution of the overstress (i.e, stable creep). By contrast, the viscoplastic localization criterion of simulation P4 always evolves within a domain characterized by positive  $H_{IN}$ . As a result, the eigenvalues of matrix  $\mathbf{Z}$  in Eq. 15 are correspondingly negative, which underpins decaying strain rate and stable creep response.

In this work, the well-known accelerating creep near failure was not simulated because the constitutive model used here is optimized to cope with compaction processes in the cap region of porous rocks. This aspect has indeed distinct features compared to traditional failure processes, in that it involves localization instability strictly inside the shear failure domain, and so more challenging to capture. However, it should be noted that the accelerating creep near failure can also be captured by the proposed criteria. As a consequence, use of the proposed relations with different viscoplastic constitutive laws specifically optimized to address brittle failure is possible, without major changes in the methodology.

## 5 Finite Element Simulation of Strain Localization

In Section 4, simple shear constraints at the material point level were used to simulate the local response leading to strain localization. In order to examine different potential band inclinations, such constraints were imposed within a locally rotated reference system.

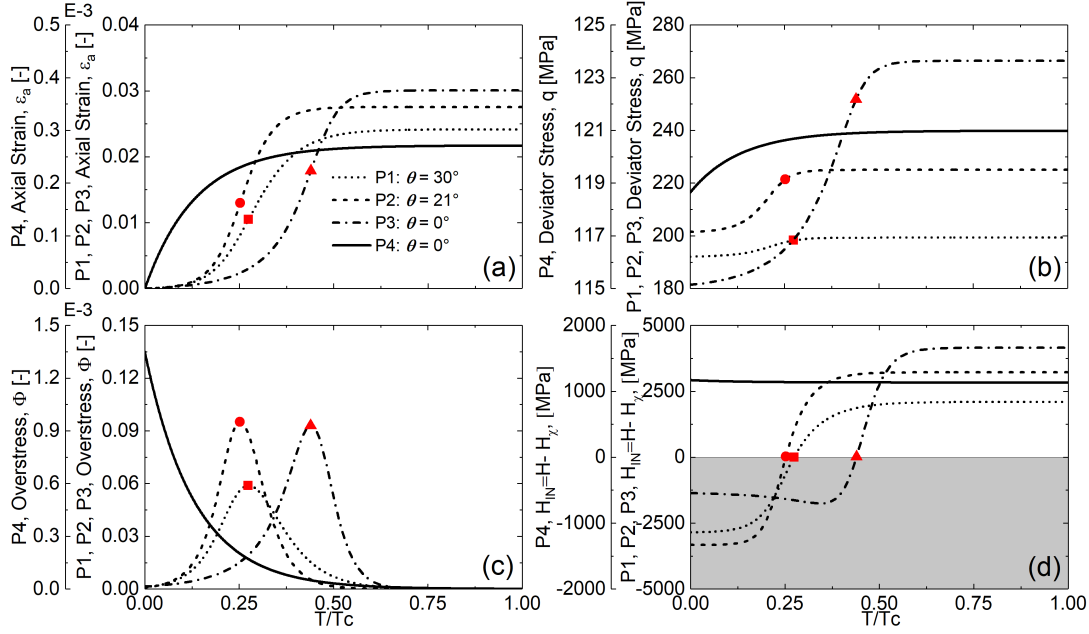


Figure 5: Analyses of simple shear creep preceded by oedometric loading: (a) Evolution of axial strain during creep, (b) Evolution of deviatoric stress, (c) Mobilized overstress, and (d) History of the viscoplastic localization criterion  $H_{IN}$  during creep for the four stress paths. T and  $T_c$  are the current creep time and total creep time, respectively.

This strategy, however, is only a simplification of real boundary value problems. The theory should therefore be tested in light of full-field analyses, which are here conducted through the finite element method. The elasto-viscoplastic constitutive model presented in Section 3 was implemented in the Abaqus UMAT interface following a strategy similar to that detailed by [82]. Fig. 6a shows the geometry, boundary conditions, and discretized meshes of the plane strain sample, the dimensions of which are  $4\text{mm} \times 2\text{mm}$ . The sample is discretized with 12800 C3D8 elements. The nodes along both lateral sides of the sample are constrained from moving horizontally and the vertical displacements are fixed at the base. The sample is subjected to a prescribed vertical displacement at the top (the axial strain rate is set to  $1.0e^{-5}s^{-1}$ , in accordance with those in experiments) to bring the stress state of each Gauss point within the domain to reach the yield surface approximately, and then the traction at the top is kept constant to make sure the sample can creep over time under stationary external perturbations. To trigger strain localization, a weak region with 95% hydrostatic yielding pressure (i.e., 95% $P^*$ ) was set at the middle of the sample. It is known that strain localization generates mesh dependency in full-field finite element simulations based on classical rate-independent continuum models. In this paper, The use of viscoplastic regularization can overcome this issue and obtain mesh objectivity, as shown in Appendix. C.

The mechanical responses under varied confining pressures (i.e.,  $P_0 = 10\text{MPa}$ ,  $40\text{MPa}$ ,  $140\text{MPa}$ , and  $250\text{MPa}$ , the same as those used in section 4) are shown in Fig. 6b; the beginning of the creep stage is marked by a gray star. It can be seen from Fig. 6b that during the creep stage the nominal deviator stress is kept constant as the strain evolves. Strain fields computed in the four simulations are reported in Fig. 7. The strain field

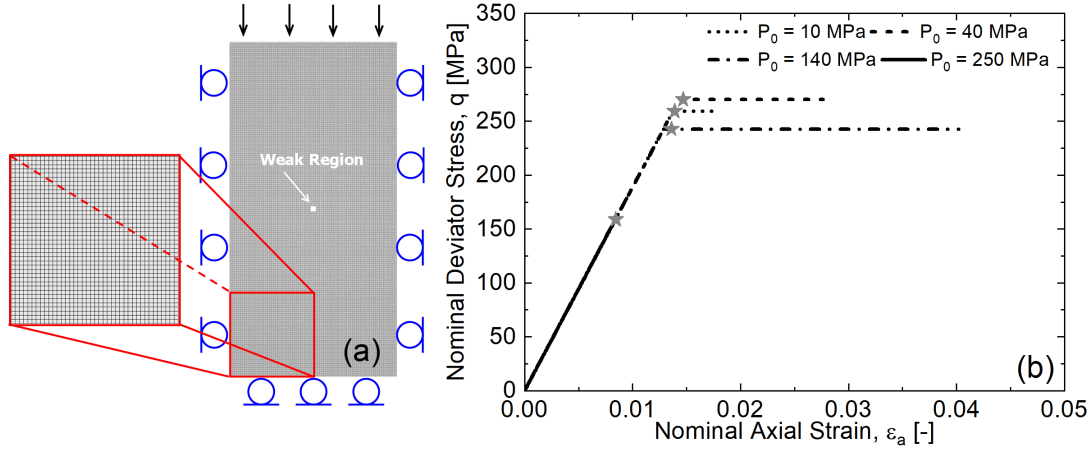


Figure 6: Numerical simulations of the plane strain sample: (a) Geometry, boundary conditions, and discretized meshes and (b) Mechanical responses

is reported in form of volumetric plastic strain. It can be observed that all specimens compressed in the strain localization regime displayed deformation bands as soon as the stress state enters into the plastic domain ( $T/T_c = 0$ ), as shown in Figs. 7a through 7c. The inclination of the bands varies depending on the confining pressure. The bands have inclination angles that are quite consistent with theoretical predictions ( $30^\circ$ ,  $21^\circ$ , and  $0^\circ$  under, respectively,  $P_0 = 10\text{MPa}$ ,  $40\text{MPa}$ , and  $140\text{MPa}$ ), indicating that the localization modes are shear band, shear-enhanced compaction band, and pure compaction band, respectively. Deformation bands with similar features have been observed in several laboratory experiments on porous sandstones [42, 43, 51, 54]. Figs. 7a through 7c also show the spatial propagation of strain localization during constant-traction creep stage. Overall, the propagation mode of volumetric plastic strain for  $P_0 = 10\text{MPa}$ ,  $40\text{MPa}$ , and  $140\text{MPa}$  is similar, i.e., initiates from the weak region and then propagated spatially to the vertical boundaries of the sample along specific inclinations predicted by the theory. Besides, the thickness of the localized band increases significantly as the inclination decreases. By contrast, the strain field obtained using  $P_0 = 250\text{MPa}$  show a diffusive deformation mode, instead of forming strain localized bands. The results show that the local theory can satisfactorily reflect the characteristics of the volumetric plastic strain field at the onset of strain localization (i.e., quasi-quasi-instantaneous strain localization).

Local responses are recovered from Gauss points located inside (a) the initially activated plastic zone (i.e., activated at  $T/T_c = 0.0$ ) and (b) the subsequently developed plastic zone (i.e., developed during  $T/T_c = 0.2$  through  $1.0$ ). The two Gauss points are marked by a red star and a yellow star, respectively, as shown in Figs. 8, 9, 10, and 11. The evolution of the axial strain, overstress, and viscoplastic localization criterion are reported during the creep stage. The stress paths of the selected Gauss points are shown in Figs. 8a, 9a, 10a, and 11a. It can be observed that for all cases the evolution trends of stress paths are similar to their counterparts in section 4. Figs. 8b, 9b, and 10b show the evolution of axial strain produced during the creep stage for  $P_0 = 10\text{MPa}$ ,  $40\text{MPa}$ , and  $140\text{MPa}$ . The obtained result of all Gauss points, especially the yellow star marked points, show an initial accelerating trend (i.e., unstable), followed by a subsequent deceleration trend (i.e., stable). By contrast, the creep strain rate of  $P_0 = 250\text{MPa}$ , however, always

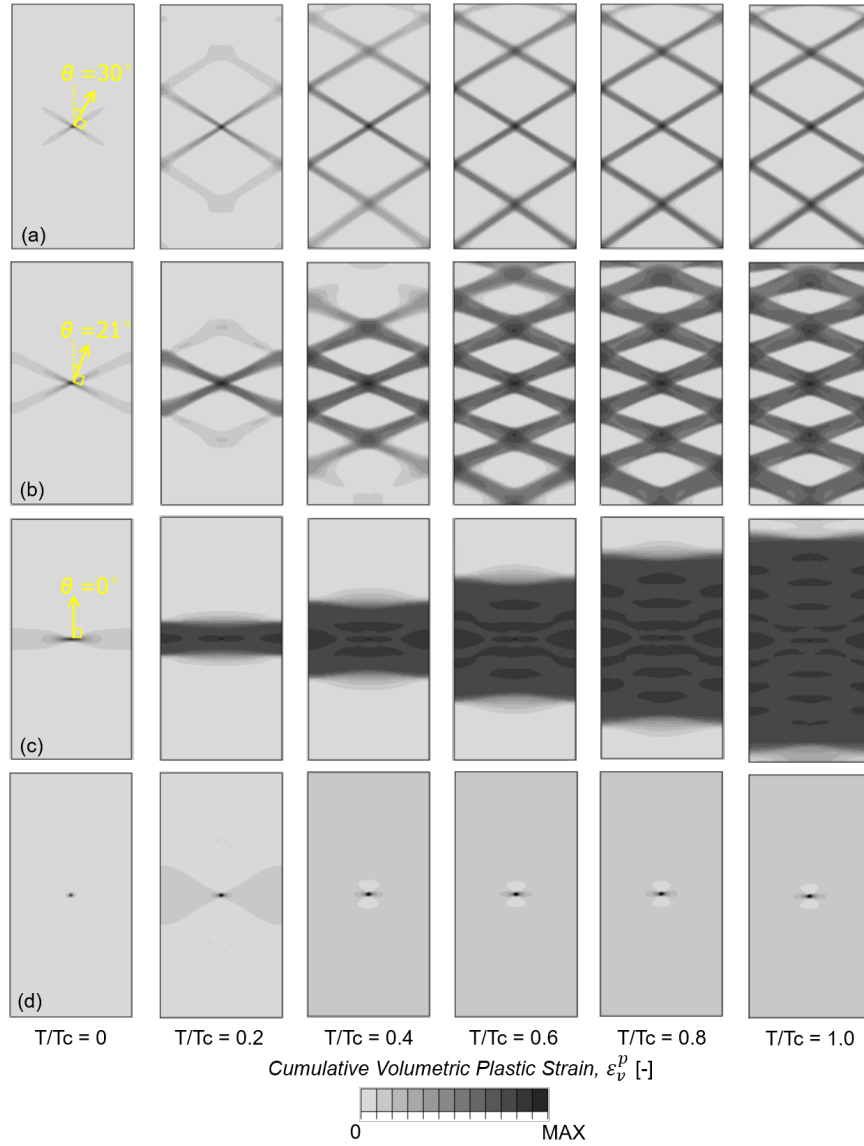


Figure 7: Cumulative volumetric plastic strain contours of the constant-stress creep simulations with confining pressure of (a)  $P_0 = 10MPa$ , (b)  $P_0 = 40MPa$ , (c)  $P_0 = 140MPa$ , and (d)  $P_0 = 250MPa$ . Cumulative volumetric plastic strain here represents the computed total volumetric plastic strain along simulations.

show a decaying trend, as shown in Fig. 11b. The unstable and stable strain response inside the localized band is related to the sharp increase and steep drop in the history of overstress, as shown in Figs. 8c, 9c, 10c, and 11c. The unstable and stable strain response inside the plastic zone is also associated with the negative and positive sign of the viscoplastic localization criterion for specific inclinations, respectively (i.e., localized bands with inclinations of  $30^\circ$ ,  $21^\circ$ , and  $0^\circ \rightarrow H_{IN}(\theta = 30^\circ)$ ,  $H_{IN}(\theta = 21^\circ)$ , and  $H_{IN}(\theta = 0^\circ)$ ), as shown in Figs. 8d, 9d, and 10d). For  $P_0 = 250\text{MPa}$ , the stable evolution of the local deformation response always corresponds to positive  $H_{IN}(\theta = 0^\circ)$ , which is the minimum value of  $H_{IN}(\theta = 0^\circ \sim 180^\circ)$ . By comparing the evolution of overstress and viscoplastic localization criterion for  $P_0 = 10\text{MPa}$ ,  $40\text{MPa}$ , and  $140\text{MPa}$ , the peak of the overstress always corresponds to a sign transition of  $H_{IN}$  (from negative to positive) for the considered band inclination. The full-field numerical simulations and corresponding analyses presented in this section reveal that the proposed viscoplastic localization criterion can satisfactorily be used to examine both quasi-instantaneous (i.e., load-induced) strain localization for general band angles, as well as delayed band propagation patterns caused by locally unstable creep response.

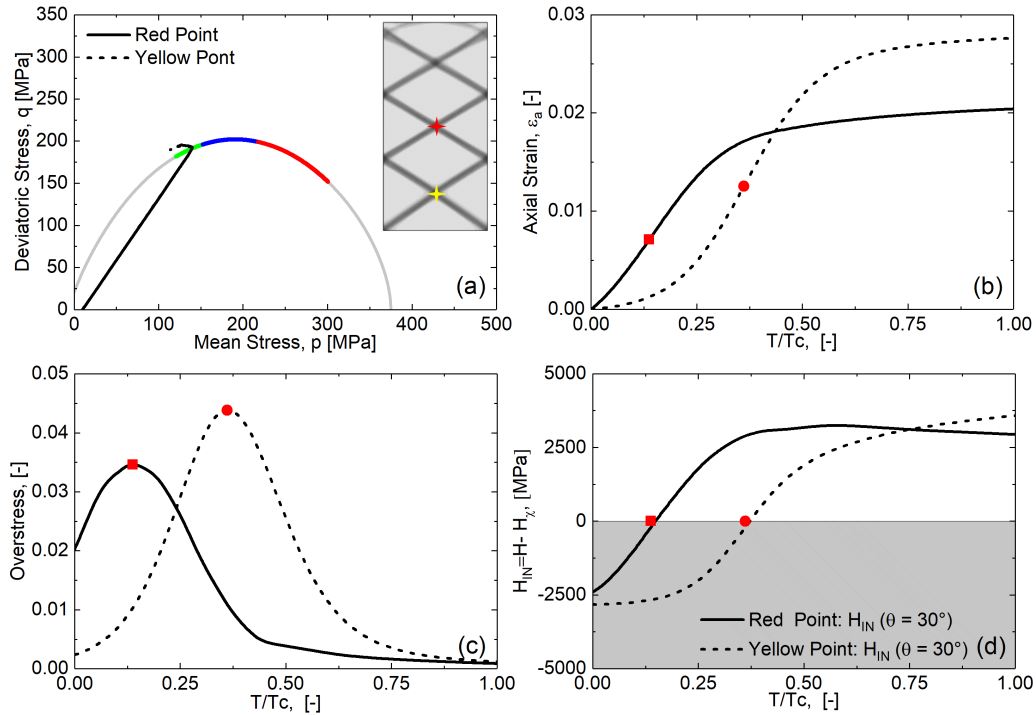


Figure 8: Gauss point analyses extracted from the full-field simulations under the confining pressure of  $P_0 = 10\text{MPa}$ : (a) Stress paths of red Gauss point and yellow Gauss point, (b) Evolution of the axial strain during the creep stage, (c) Evolution of the viscoplastic localization criterion  $H_{IN}$  during the creep stage, and (d) Evolution of the overstress,  $\Phi$ .

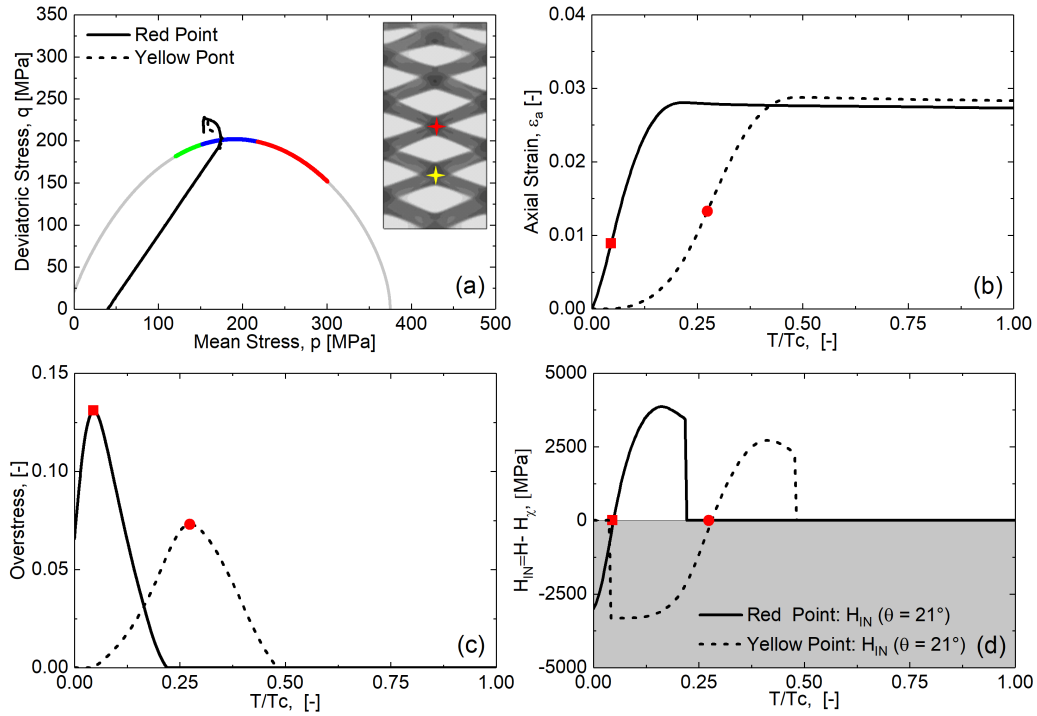


Figure 9: Gauss point analyses extracted from the full-field simulations under the confining pressure of  $P_0 = 40MPa$ : (a) Stress paths of red Gauss point and yellow Gauss point, (b) Evolution of the axial strain during the creep stage, (c) Evolution of the viscoplastic localization criterion  $H_{IN}$  during the creep stage, and (d) Evolution of the overstress,  $\Phi$ .

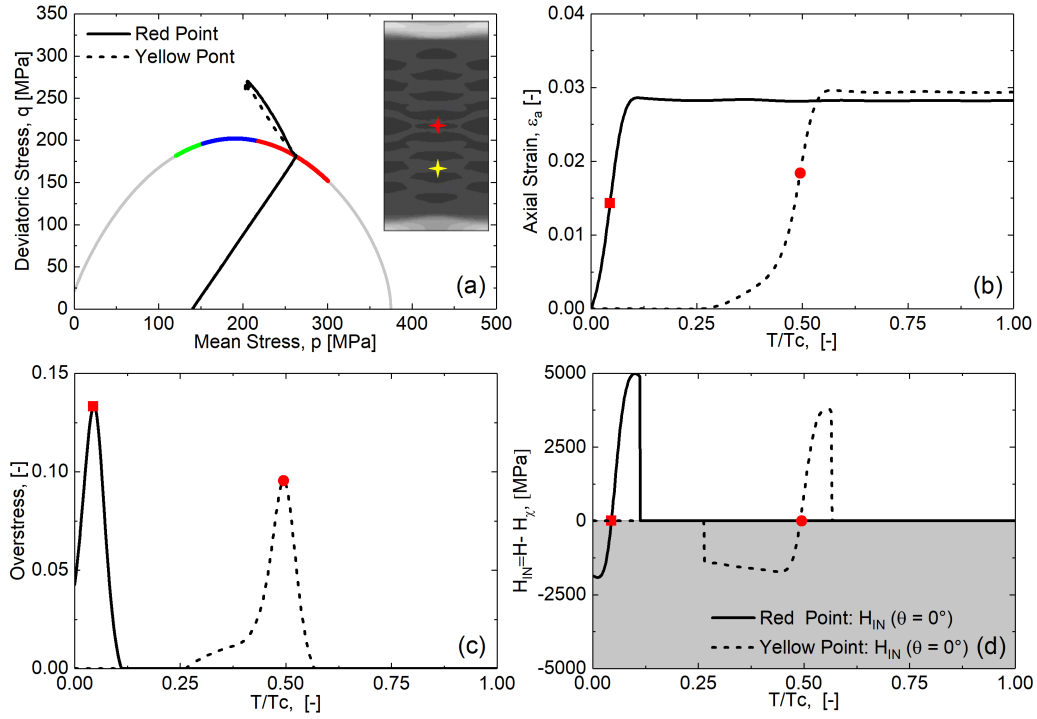


Figure 10: Gauss point analyses extracted from the full-field simulations under the confining pressure of  $P_0 = 140 \text{ MPa}$ : (a) Stress paths of red Gauss point and yellow Gauss point, (b) Evolution of the axial strain during the creep stage, (c) Evolution of the viscoplastic localization criterion  $H_{IN}$  during the creep stage, and (d) Evolution of the overstress,  $\Phi$ .

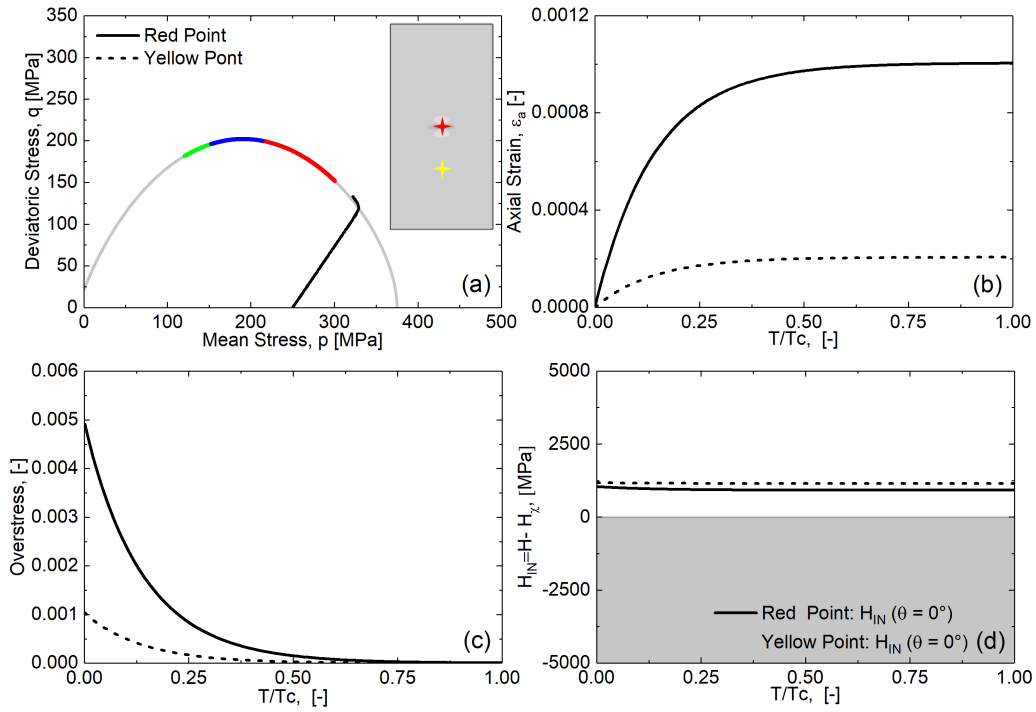


Figure 11: Gauss point analyses extracted from the full-field simulations under the confining pressure of  $P_0 = 250\text{MPa}$ : (a) Stress paths of red Gauss point and yellow Gauss point, (b) Evolution of the axial strain during the creep stage, (c) Evolution of the viscoplastic localization criterion  $H_{IN}$  during the creep stage, and (d) Evolution of the overstress,  $\Phi$ .

## 6 Conclusions

This paper has presented a versatile viscoplastic localization criterion for characterizing the inception of quasi-instantaneous (i.e., load-induced) and delayed unstable strain localization in rate-dependent solids. For this purpose, a system of ordinary differential equations (OEDs) governing the temporal evolution of the response variables describing creep-induced strain localization is formulated based on viscoplasticity and the control conditions inside an active band. This viscoplastic localization criterion relates to the eigenvalues of the governing constitutive operator of the OEDs system, and can be used to identify the unstable or stable material response inside spontaneously propagating deformation bands under stationary external loading. Using a non-associative strain-hardening elasto-viscoplastic model able to capture different modes of strain localization, strain localization analyses by constitutive equations are conducted at the material point level to show that the onset of different modes of strain localization predicted by the proposed theory agrees with classic predictions of the standard strain localization theory for rate-independent elastoplastic solids. This indicates the applicability of the theory on capturing quasi-instantaneous strain localization. The acceleration and deceleration of the response variables during the creep simulations is caused by the relative movement between the stress state exceeding the elastic domain and yield surface, which is associated with the increasing and decreasing of overstress, respectively. The sign change of the viscoplastic localization criterion presented in this paper (from negative to positive) corresponds to the transition point at which the evolution of response variables shifts from accelerating to decelerating, and is also associated with the peak of overstress. These results indicate that the proposed viscoplastic localization criterion is a useful tool to explain transitions from unstable to stable (and viceversa) local deformation response. The full-field numerical simulations have further corroborated these predictions. In fact, during the creep stage, the strain evolution at local Gauss points shows an initial unstable accelerating response followed by a subsequent stable decelerating response. The peak of the overstress, which is related to the transition point of unstable and stable strain response, was found to agree with the sign change (from negative to positive) of the local viscoplastic localization criterion for specific band inclinations, thus demonstrating the applicability of the proposed criterion for the inspection of onset, propagation and arrest of localized deformation zones.

## Acknowledgement

This work was primarily supported by the U.S. Department of Energy (grant no. DE-SC0017615) awarded to Giuseppe Buscarnera. Dawei Xue also kindly acknowledges the support of China Scholarship Council for his overseas studies.

## A The deformation kinematic of strain localization

In this paper, we assume that the kinematics of deformation inside the active bands is consistent with simple shear conditions. As a result, the stress rate  $\dot{\sigma}_{11}$ , perpendicular to the band, and  $\dot{\tau}_{12}$ , parallel to the shear direction, are regarded as directly controlled, in that associated with local equilibrium conditions. In addition to controlled stresses, kinematic constraints include the requirement of plane-strain conditions, i.e.,  $\dot{\epsilon}_{33} = \dot{\gamma}_{13} = \dot{\gamma}_{23} = 0$ , and zero extensional strain along the shear direction, i.e.,  $\dot{\epsilon}_{22} = 0$ . Within the context of

controllability analyses, these constrain constitute the full set of control conditions. As a result, the control variables are:

$$\begin{Bmatrix} \dot{\sigma}_{\alpha} \\ \dot{\epsilon}_{\beta} \end{Bmatrix} = \begin{Bmatrix} \dot{\sigma}_{11} \\ \dot{\tau}_{12} \\ \dot{\epsilon}_{22} \\ \dot{\epsilon}_{33} \\ \dot{\gamma}_{23} \\ \dot{\gamma}_{13} \end{Bmatrix} \quad (\text{A.1})$$

while, their corresponding response variables are:

$$\begin{Bmatrix} \dot{\epsilon}_{\alpha} \\ \dot{\sigma}_{\beta} \end{Bmatrix} = \begin{Bmatrix} \dot{\epsilon}_{11} \\ \dot{\gamma}_{12} \\ \dot{\sigma}_{22} \\ \dot{\sigma}_{33} \\ \dot{\tau}_{23} \\ \dot{\tau}_{13} \end{Bmatrix} \quad (\text{A.2})$$

As mentioned in the previous section, it is convenient to impose these conditions within the reference system of the band. This procedure facilitates the analysis of strain localization initiation and progression for arbitrary band inclinations. Such procedure involves a directional cosine matrix,  $\mathbf{T}$ , which converts the constitutive equations into a Cartesian reference frame aligned with the band. Matrix  $\mathbf{T}$  is defined as follows:

$$\mathbf{T} = \begin{bmatrix} l_{11}^2 & l_{12}^2 & l_{13}^2 & 2l_{11}l_{12} & 2l_{12}l_{13} & 2l_{11}l_{13} \\ l_{21}^2 & l_{22}^2 & l_{23}^2 & 2l_{21}l_{22} & 2l_{22}l_{23} & 2l_{21}l_{23} \\ l_{31}^2 & l_{32}^2 & l_{33}^2 & 2l_{31}l_{32} & 2l_{32}l_{33} & 2l_{31}l_{33} \\ l_{11}l_{21} & l_{12}l_{22} & l_{13}l_{23} & (l_{11}l_{22} + l_{12}l_{21}) & (l_{12}l_{23} + l_{13}l_{22}) & (l_{11}l_{23} + l_{13}l_{21}) \\ l_{21}l_{31} & l_{22}l_{32} & l_{23}l_{33} & (l_{21}l_{32} + l_{22}l_{31}) & (l_{22}l_{33} + l_{23}l_{32}) & (l_{21}l_{33} + l_{23}l_{31}) \\ l_{11}l_{31} & l_{12}l_{32} & l_{13}l_{33} & (l_{11}l_{32} + l_{12}l_{31}) & (l_{12}l_{33} + l_{13}l_{32}) & (l_{11}l_{33} + l_{13}l_{31}) \end{bmatrix} \quad (\text{A.3})$$

where,  $l_{ij}$  are the components of matrix  $\mathbf{L}$ , defined as:

$$\mathbf{L} = \begin{bmatrix} \cos \theta & \sin \theta & 0 \\ -\sin \theta & \cos \theta & 0 \\ 0 & 0 & 1 \end{bmatrix} \quad (\text{A.4})$$

in which,  $\theta$  is the angle of clockwise rotation around the out of plane direction, also referred to as the inclination of the deformation band.

## B Expression of the modulus of controllability $H_{\chi}$

The aim of this appendix is to show technical details for computing the modulus of controllability  $H_{\chi}$  to ease the practical use of the criterion for readers. According to Eqs. 11 and 7a,  $H_{\chi}$  is expressed as follows:

$$H_{\chi} = -\frac{\partial f}{\partial \sigma_{\beta}^R} \mathbf{T} \left[ \mathbf{D}_{\beta\beta}^{e,R} + \mathbf{D}_{\beta\alpha}^{e,R} (\mathbf{D}_{\alpha\alpha}^{e,R})^{-1} \mathbf{D}_{\alpha\beta}^{e,R} \right] \frac{\partial g}{\partial \sigma_{\beta}^R} \quad (\text{B.1})$$

where,  $\frac{\partial f}{\partial \sigma_{\beta}^R}$  and  $\frac{\partial g}{\partial \sigma_{\beta}^R}$  can be computed according to the following equation:

$$\frac{\partial h}{\partial \sigma_{\beta}^R} = \begin{Bmatrix} \frac{\partial h}{\partial \sigma_{\alpha}^R} \\ \frac{\partial h}{\partial \sigma_{\beta}^R} \end{Bmatrix} = (\mathbf{T}^T)^{-1} \begin{Bmatrix} \frac{\partial h}{\partial \sigma_{\alpha}} \\ \frac{\partial h}{\partial \sigma_{\beta}} \end{Bmatrix} = (\mathbf{T}^T)^{-1} (\mathbf{T}_{\sigma}^T)^{-1} \frac{\partial h}{\partial \sigma_{ij}} \quad (\text{B.2})$$

where,  $\mathbf{T}$  is the directional cosine matrix given by Eq. A.3,  $h$  makes reference to either the yield surface ( $h \Rightarrow f$ ) or the plastic potential ( $h \Rightarrow g$ ), and  $\mathbf{T}_{\sigma}$  is a transformation matrix to recast the order of components in the original stress vector from  $\{\sigma_{11} \ \sigma_{22} \ \sigma_{33} \ \tau_{12} \ \tau_{23} \ \tau_{13}\}^T$  to  $\{\sigma_{11} \ \tau_{12} \ \sigma_{22} \ \sigma_{33} \ \tau_{23} \ \tau_{13}\}^T$ . It should be noted here that  $\{\sigma_{11} \ \tau_{12}\}^T$  represents the vector  $\sigma_{\alpha}$ , while  $\{\sigma_{22} \ \sigma_{33} \ \tau_{23} \ \tau_{13}\}^T$  represents the vector  $\sigma_{\beta}$ .  $\mathbf{T}_{\sigma}$  is given by:

$$\mathbf{T}_{\sigma} = \begin{Bmatrix} 1 & 0 & 0 & 0 & 0 & 0 \\ 0 & 0 & 0 & 1 & 0 & 0 \\ 0 & 1 & 0 & 0 & 0 & 0 \\ 0 & 0 & 1 & 0 & 0 & 0 \\ 0 & 0 & 0 & 0 & 1 & 0 \\ 0 & 0 & 0 & 0 & 0 & 1 \end{Bmatrix} \quad (\text{B.3})$$

Then,  $\frac{\partial h}{\partial \sigma_{\beta}^R}$  can be obtained by taking the last four components in the vector  $\frac{\partial h}{\partial \sigma^R}$ .

The computation of  $D_{\alpha\alpha}^{e,R}$ ,  $D_{\alpha\beta}^{e,R}$ ,  $D_{\beta\alpha}^{e,R}$ , and  $D_{\beta\beta}^{e,R}$  can be implemented according to the following equation:

$$D^{e,R} = \begin{Bmatrix} D_{\alpha\alpha}^{e,R} & D_{\alpha\beta}^{e,R} \\ D_{\beta\alpha}^{e,R} & D_{\beta\beta}^{e,R} \end{Bmatrix} = \mathbf{T} \begin{Bmatrix} D_{\alpha\alpha}^e & D_{\alpha\beta}^e \\ D_{\beta\alpha}^e & D_{\beta\beta}^e \end{Bmatrix} \mathbf{T}^{-1} = \mathbf{T} \mathbf{T}_{\sigma} \{D_{ijkl}^e\} \mathbf{T}_{\sigma}^{-1} \mathbf{T}^{-1} \quad (\text{B.4})$$

where,  $D_{ijkl}^e$  is the elastic tensor given by Eq. 27.  $D_{\alpha\alpha}^{e,R}$ ,  $D_{\alpha\beta}^{e,R}$ ,  $D_{\beta\alpha}^{e,R}$ , and  $D_{\beta\beta}^{e,R}$  can be obtained by taking the top-left corner  $2 \times 2$  sub-matrix, top-right corner  $2 \times 4$  sub-matrix, bot-left  $4 \times 2$  sub-matrix, and bot-right  $4 \times 4$  sub-matrix in the matrix  $D^{e,R}$ , respectively. Analogy, the partitioned elastic tensors  $D_{\alpha\beta}^e$ ,  $D_{\beta\alpha}^e$ , and  $D_{\beta\beta}^e$  shown in Eq. 1 can be obtained by taking the top-left corner  $2 \times 2$  sub-matrix, top-right corner  $2 \times 4$  sub-matrix, bot-left  $4 \times 2$  sub-matrix, and bot-right  $4 \times 4$  sub-matrix in the matrix  $\mathbf{T}_{\sigma} \{D_{ijkl}^e\} \mathbf{T}_{\sigma}^{-1}$ , respectively.

## C Mesh sensitivity analysis

When analyzing strain localization bands in finite element simulations, the use of classical continuum models typically suffers from mesh dependency. Specifically, finite element simulations show a reduction of localized zone thicknesses upon mesh refinement, which violates physical observations. In this appendix, quarter plane strain compression test sample is used to verify that the use of viscoplastic regularization is able to gain mesh objectivity, as shown in Fig. C.1. For different meshes, the overall mechanical responses are comparable and the thicknesses of strain localization zones are consistent.

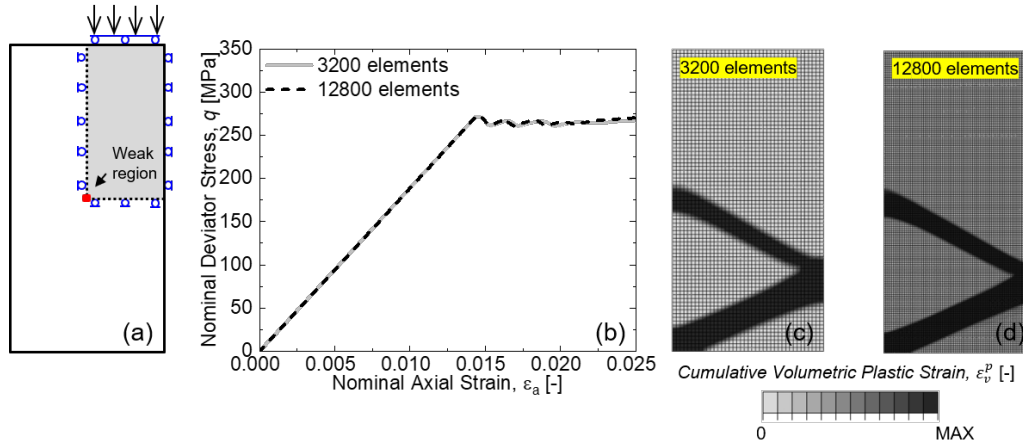


Figure C.1: Mesh sensitivity analysis through quarter plane strain compression sample (confining pressure  $P_0 = 40\text{MPa}$ ): (a) finite element model, (b) mechanical responses, and (c-d) cumulative volumetric plastic strain contours from coarse mesh and fine mesh.

## Data Availability Statement

Data sharing is not applicable to this article as no new data was generated during the current study.

## References

- [1] Ikeda K, Yamakawa Y, Desrues J, Murota K. Bifurcations to diversify geometrical patterns of shear bands on granular material. *Physical review letters*. 2008;100(19):198001.
- [2] Goddard JD. Continuum modeling of granular media. *Applied Mechanics Reviews*. 2014;66(5).
- [3] Alshibli KA, Batiste SN, Sture S. Strain localization in sand: plane strain versus triaxial compression. *Journal of Geotechnical and Geoenvironmental Engineering*. 2003;129(6):483-94.
- [4] Desrues J. Tracking strain localization in geomaterials using computerized tomography. *X-ray CT for Geomaterials*. 2004:15-41.
- [5] McBeck JA, Cordonnier B, Vinciguerra S, Renard F. Volumetric and shear strain localization in Mt. Etna basalt. *Geophysical Research Letters*. 2019;46(5):2425-33.
- [6] Salvatore E, Spacagna R, Andò E, Ochmanski M. Geostatistical analysis of strain localization in triaxial tests on sand. *Géotechnique Letters*. 2019;9(4):334-9.
- [7] Alsaleh MI, Voyiadjis GZ, Alshibli KA. Modelling strain localization in granular materials using micropolar theory: mathematical formulations. *International journal for numerical and analytical methods in geomechanics*. 2006;30(15):1501-24.

- [8] Chen Q, Andrade JE, Samaniego E. AES for multiscale localization modeling in granular media. *Computer Methods in Applied Mechanics and Engineering*. 2011;200(33-36):2473-82.
- [9] Shahin G, Papazoglou A, Marinelli F, Buscarnera G. Simulation of localized compaction in Tuffeau de Maastricht based on evidence from X-ray tomography. *International Journal of Rock Mechanics and Mining Sciences*. 2019;121:104039.
- [10] Nguyen GD, Bui HH. A thermodynamics-and mechanism-based framework for constitutive models with evolving thickness of localisation band. *International Journal of Solids and Structures*. 2020;187:100-20.
- [11] Lü X, Xue D, Lim KW. Implicit gradient softening plasticity for the modeling of strain localization in soils. *Computer Methods in Applied Mechanics and Engineering*. 2020;364:112934.
- [12] Hill R, Hutchinson J. Bifurcation phenomena in the plane tension test. *Journal of the Mechanics and Physics of Solids*. 1975;23(4-5):239-64.
- [13] Pijaudier-Cabot G, Benallal A. Strain localization and bifurcation in a nonlocal continuum. *International Journal of Solids and Structures*. 1993;30(13):1761-75.
- [14] Song X. Transient bifurcation condition of partially saturated porous media at finite strain. *International Journal for Numerical and Analytical Methods in Geomechanics*. 2017;41(1):135-56.
- [15] Hill R. A general theory of uniqueness and stability in elastic-plastic solids. *Journal of the Mechanics and Physics of Solids*. 1958;6(3):236-49.
- [16] Rudnicki JW, Rice J. Conditions for the localization of deformation in pressure-sensitive dilatant materials. *Journal of the Mechanics and Physics of Solids*. 1975;23(6):371-94.
- [17] Papamichos E, Vardoulakis I. Shear band formation in sand according to non-coaxial plasticity model. *Geotechnique*. 1995;45(4):649-61.
- [18] Huang M, Lu X, Qian J. Non-coaxial elasto-plasticity model and bifurcation prediction of shear banding in sands. *International journal for numerical and analytical methods in geomechanics*. 2010;34(9):906-19.
- [19] Yang Y, Yu H. A non-coaxial critical state soil model and its application to simple shear simulations. *International journal for numerical and analytical methods in geomechanics*. 2006;30(13):1369-90.
- [20] Lü X, Huang M, Qian J. Prediction of plane strain undrained diffuse instability and strain localization with non-coaxial plasticity. *Soils and Foundations*. 2014;54(6):1070-1080. Available from: <http://www.sciencedirect.com/science/article/pii/S0038080614001218>.
- [21] Gao Z, Zhao J. A non-coaxial critical-state model for sand accounting for fabric anisotropy and fabric evolution. *International Journal of Solids and Structures*. 2017;106:200-12.

- [22] Lü X, Huang M, Qian J. Influences of loading direction and intermediate principal stress ratio on the initiation of strain localization in cross-anisotropic sand. *Acta Geotechnica*. 2018;13(3):619-33.
- [23] Nicot F, Darve F, Dat Vu Khoa H. Bifurcation and second-order work in geomaterials. *International journal for numerical and analytical methods in geomechanics*. 2007;31(8):1007-32.
- [24] Wan R, Pinheiro M, Daouadji A, Jrad M, Darve F. Diffuse instabilities with transition to localization in loose granular materials. *International Journal for Numerical and Analytical Methods in Geomechanics*. 2013;37(10):1292-311.
- [25] Marinelli F, Buscarnera G. Parameter calibration for high-porosity sandstones deformed in the compaction banding regime. *International Journal of Rock Mechanics and Mining Sciences*. 2015;78:240-52.
- [26] Chen Z, Huang M. Non-coaxial behavior modeling of sands subjected to principal stress rotation. *Acta Geotechnica*. 2020;15(3):655-69.
- [27] Makhnenko RY, Ge C, Labuz JF. Localization of deformation in fluid-saturated sandstone. *International Journal of Rock Mechanics and Mining Sciences*. 2020;134:104455.
- [28] Nova R. Controllability of the incremental response of soil specimens subjected to arbitrary loading programmes. *Journal of the Mechanical behavior of Materials*. 1994;5(2):193-202.
- [29] Hu G, Yang J, Liu W. Instability and controllability of linearly coupled oscillators: Eigenvalue analysis. *Physical Review E*. 1998;58(4):4440.
- [30] Buscarnera G, Dattola G, Di Prisco C. Controllability, uniqueness and existence of the incremental response: A mathematical criterion for elastoplastic constitutive laws. *International Journal of Solids and Structures*. 2011;48(13):1867-78.
- [31] Mihalache C, Buscarnera G. Mathematical identification of diffuse and localized instabilities in fluid-saturated sands. *International Journal for Numerical and Analytical Methods in Geomechanics*. 2014;38(2):111-41.
- [32] Lajtai E, Schmidtke R. Delayed failure in rock loaded in uniaxial compression. *Rock mechanics and rock engineering*. 1986;19(1):11-25.
- [33] Oka F, Adachi T, Yashima A. Instability of an elasto-viscoplastic constitutive model for clay and strain localization. *Mechanics of materials*. 1994;18(2):119-29.
- [34] Noda T, Fernando G, Asaoka A. Delayed failure in soft clay foundations. *Soils and foundations*. 2000;40(1):85-97.
- [35] Kimoto S, Oka F, Higo Y. Strain localization analysis of elasto-viscoplastic soil considering structural degradation. *Computer Methods in Applied Mechanics and Engineering*. 2004;193(27-29):2845-66.
- [36] Enomoto T, Koseki J, Tatsuoka F, Sato T. Creep failure of natural gravelly soil and its simulation. *Géotechnique*. 2016;66(11):865-77.

- [37] Xu Wj, Yue Zq, Hu Rl. Study on the mesostructure and mesomechanical characteristics of the soil–rock mixture using digital image processing based finite element method. *International Journal of Rock Mechanics and Mining Sciences*. 2008;45(5):749-62.
- [38] Wen BP, Jiang XZ. Effect of gravel content on creep behavior of clayey soil at residual state: implication for its role in slow-moving landslides. *Landslides*. 2017;14(2):559-76.
- [39] Wang S, Wang J, Wu W, Cui D, Su A, Xiang W. Creep properties of clastic soil in a reactivated slow-moving landslide in the Three Gorges Reservoir Region, China. *Engineering Geology*. 2020;267:105493.
- [40] Bésuelle P. Compacting and dilating shear bands in porous rock: Theoretical and experimental conditions. *Journal of Geophysical Research: Solid Earth*. 2001;106(B7):13435-42.
- [41] Klein E, Baud P, Reuschlé T, Wong T. Mechanical behaviour and failure mode of Bentheim sandstone under triaxial compression. *Physics and Chemistry of the Earth, Part A: Solid Earth and Geodesy*. 2001;26(1-2):21-5.
- [42] Baud P, Klein E, Wong Tf. Compaction localization in porous sandstones: spatial evolution of damage and acoustic emission activity. *Journal of Structural Geology*. 2004;26(4):603-24.
- [43] Baud P, Vajdova V, Wong Tf. Shear-enhanced compaction and strain localization: Inelastic deformation and constitutive modeling of four porous sandstones. *Journal of Geophysical Research: Solid Earth*. 2006;111(B12).
- [44] Sulem J, Ouffroukh H. Shear banding in drained and undrained triaxial tests on a saturated sandstone: Porosity and permeability evolution. *International Journal of Rock Mechanics and Mining Sciences*. 2006;43(2):292-310.
- [45] Tembe S, Baud P, Wong Tf. Stress conditions for the propagation of discrete compaction bands in porous sandstone. *Journal of Geophysical Research: Solid Earth*. 2008;113(B9).
- [46] Cnudde V, Boone MN. High-resolution X-ray computed tomography in geosciences: A review of the current technology and applications. *Earth-Science Reviews*. 2013;123:1-17.
- [47] Mathews JP, Campbell QP, Xu H, Halleck P. A review of the application of X-ray computed tomography to the study of coal. *Fuel*. 2017;209:10-24.
- [48] McBeck J, Kobchenko M, Hall SA, Tudisco E, Cordonnier B, Meakin P, et al. Investigating the onset of strain localization within anisotropic shale using digital volume correlation of time-resolved X-ray microtomography images. *Journal of Geophysical Research: Solid Earth*. 2018;123(9):7509-28.
- [49] Ju Y, Xi C, Zhang Y, Mao L, Gao F, Xie H. Laboratory in situ CT observation of the evolution of 3D fracture networks in coal subjected to confining pressures and axial compressive loads: a novel approach. *Rock Mechanics and Rock Engineering*. 2018;51(11):3361-75.

- [50] Huang L, Baud P, Cordonnier B, Renard F, Liu L, Wong Tf. Synchrotron X-ray imaging in 4D: Multiscale failure and compaction localization in triaxially compressed porous limestone. *Earth and Planetary Science Letters*. 2019;528:115831.
- [51] Brantut N, Heap M, Meredith P, Baud P. Time-dependent cracking and brittle creep in crustal rocks: A review. *Journal of Structural Geology*. 2013;52:17-43.
- [52] Brantut N, Heap M, Baud P, Meredith P. Rate-and strain-dependent brittle deformation of rocks. *Journal of Geophysical Research: Solid Earth*. 2014;119(3):1818-36.
- [53] Li X, Shao Z. Investigation of macroscopic brittle creep failure caused by microcrack growth under step loading and unloading in rocks. *Rock Mechanics and Rock Engineering*. 2016;49(7):2581-93.
- [54] Heap MJ, Brantut N, Baud P, Meredith PG. Time-dependent compaction band formation in sandstone. *Journal of Geophysical Research: Solid Earth*. 2015;120(7):4808-30.
- [55] Nicolas A, Fortin J, Regnet J, Verberne B, Plümper O, Dimanov A, et al. Brittle and semibrittle creep of Tavel limestone deformed at room temperature. *Journal of Geophysical Research: Solid Earth*. 2017;122(6):4436-59.
- [56] Di Prisco C, Imposimato S, Aifantis E. A visco-plastic constitutive model for granular soils modified according to non-local and gradient approaches. *International journal for numerical and analytical methods in geomechanics*. 2002;26(2):121-38.
- [57] Pellet F, Hajdu A, Deleruyelle F, Besnus F. A viscoplastic model including anisotropic damage for the time dependent behaviour of rock. *International journal for numerical and analytical methods in geomechanics*. 2005;29(9):941-70.
- [58] Yin Z, Chang C, Karstunen M, Hicher PY. An anisotropic elastic-viscoplastic model for soft clays. *International Journal of Solids and Structures*. 2010;47(5):665-77.
- [59] Liu C, Zhou F, Kang J, Xia T. Application of a non-linear viscoelastic-plastic rheological model of soft coal on borehole stability. *Journal of Natural Gas Science and Engineering*. 2016;36:1303-11.
- [60] Islam M, Gnanendran C. Non-Associated Flow Rule-Based Elasto-Viscoplastic Model for Clay. *Geosciences*. 2020;10(6):227.
- [61] Perzyna P. Fundamental problems in viscoplasticity. In: *Advances in applied mechanics*. vol. 9. Elsevier; 1966. p. 243-377.
- [62] Di Prisco C, Imposimato S, Vardoulakis I. Mechanical modelling of drained creep triaxial tests on loose sand. *Geotechnique*. 2000;50(1):73-82.
- [63] Lazari M, Sanavia L, di Prisco C, Pisanò F. Predictive potential of Perzyna viscoplastic modelling for granular geomaterials. *International Journal for Numerical and Analytical Methods in Geomechanics*. 2019;43(2):544-67.
- [64] Shi Z, Hambleton JP, Buscarnera G. Bounding surface elasto-viscoplasticity: A general constitutive framework for rate-dependent geomaterials. *Journal of Engineering Mechanics*. 2019;145(3):04019002.

- [65] Zhang Y, Buscarnera G. Breakage mechanics for granular materials in surface-reactive environments. *Journal of the Mechanics and Physics of Solids*. 2018;112:89-108.
- [66] Kabwe E, Karakus M, Chanda EK. Creep constitutive model considering the over-stress theory with an associative viscoplastic flow rule. *Computers and Geotechnics*. 2020;124:103629.
- [67] Oka F, Higo Y, Kimoto S. Effect of dilatancy on the strain localization of water-saturated elasto-viscoplastic soil. *International Journal of Solids and Structures*. 2002;39(13-14):3625-47.
- [68] Bargmann S, Reddy BD, Klusemann B. A computational study of a model of single-crystal strain-gradient viscoplasticity with an interactive hardening relation. *International Journal of Solids and Structures*. 2014;51(15-16):2754-64.
- [69] de Borst R, Duretz T. On viscoplastic regularisation of strain-softening rocks and soils. *International Journal for Numerical and Analytical Methods in Geomechanics*. 2020;44(6):890-903.
- [70] Pisanò F, Di Prisco C. A stability criterion for elasto-viscoplastic constitutive relationships. *International Journal for Numerical and Analytical Methods in Geomechanics*. 2016;40(1):141-56.
- [71] Marinelli F, Buscarnera G. Instability criteria for quasi-saturated viscous soils. *International Journal for Numerical and Analytical Methods in Geomechanics*. 2018;42(3):379-400.
- [72] Marinelli F, Pisanò F, Di Prisco C, Buscarnera G. Model-based interpretation of undrained creep instability in loose sands. *Géotechnique*. 2018;68(6):504-17.
- [73] Shahin G, Buscarnera G, et al. Numerical simulation of localized compaction creep in heterogeneous porous rock. In: 53rd US Rock Mechanics/Geomechanics Symposium. American Rock Mechanics Association; 2019. .
- [74] Shahin G, Marinelli F, Buscarnera G. Viscoplastic interpretation of localized compaction creep in porous rock. *Journal of Geophysical Research: Solid Earth*. 2019;124(10):10180-96.
- [75] Zhang Y, Buscarnera G. A rate-dependent breakage model based on the kinetics of crack growth at the grain scale. *Géotechnique*. 2017;67(11):953-67.
- [76] Hill R. The essential structure of constitutive laws for metal composites and polycrystals. *Journal of the Mechanics and Physics of Solids*. 1967;15(2):79-95.
- [77] Gens A, Nova R. Conceptual bases for a constitutive model for bonded soils and weak rocks. In: *Geotechnical engineering of hard soils-soft rocks*; 1993. p. 485-94.
- [78] Nova R, Castellanza R, Tamagnini C. A constitutive model for bonded geomaterials subject to mechanical and/or chemical degradation. *International Journal for Numerical and Analytical Methods in Geomechanics*. 2003;27(9):705-32.
- [79] Lagioia R, Puzrin A, Potts D. A new versatile expression for yield and plastic potential surfaces. *Computers and Geotechnics*. 1996;19(3):171-91.

- [80] Roscoe K, Burland J. On the generalized stress-strain behaviour of wet clay. *Engineering Plasticity*. 1968;553-609.
- [81] Buscarnera G, Nova R. Modelling instabilities in triaxial testing on unsaturated soil specimens. *International journal for numerical and analytical methods in geomechanics*. 2011;35(2):179-200.
- [82] Das A, Buscarnera G. Simulation of localized compaction in high-porosity calcarenite subjected to boundary constraints. *International Journal of Rock Mechanics and Mining Sciences*. 2014;71:91-104.